# Tunable mechanochromic luminescence via surface protonation of pyridyl-substituted imidazole crystals

Kubota, Rikuto
Yuan, Yanqiu
Yoshida, Ryohei
Tachikawa, Takashi
Ito, Suguru

(Citation)
Materials Advances,3(14):5826-5835

(Issue Date)
2022-07-21

(Resource Type)
journal article

(Version)
Version of Record

(URL)
https://hdl.handle.net/20.500.14094/90009564

Materials Advances

ROYAL SOCIETY OF CHEMISTRY

PAPER

View Article Online
View Journal | View Issue

Check for updates

Cite this: *Mater. Adv.*, 2022, 3, 5826

# Tunable mechanochromic luminescence *via* surface protonation of pyridyl-substituted imidazole crystals†

Rikuto Kubota,[a] Yanqiu Yuan,[a] Ryohei Yoshida,[a] Takashi Tachikawa *[bc] and Suguru Ito *[ad]

Received 4th March 2022,
Accepted 16th May 2022

DOI: 10.1039/d2ma00256f

rsc.li/materials-advances

Over the past decade, a growing number of luminescent organic materials exhibiting mechanochromic luminescence (MCL) have been developed, but controlling the magnitude of the mechanically induced shift in emission wavelength is still a great challenge. Herein, the rational extension of the MCL shift has been achieved *via* surface protonation of pyridyl-substituted imidazole crystals **1** and **2**. The MCL shift of phenanthroimidazole **1** was 38 nm, whereas the emission wavelength of triphenylimidazole **2** was not affected by mechanical stimuli. After being treated with HCl vapor, the MCL shifts of **1** and **2** increased to 64 and 37 nm, respectively. *In situ* fluorescence microscopy has revealed that when exposed to HCl vapor, small microcrystals (1–4 μm in size) attached to the surface of a large crystal responded faster in terms of emission properties than the larger crystal. On the basis of powder X-ray diffraction analysis, spatially resolved fluorescence microscopy, and fluorescence lifetime analysis, the extended MCL shift after acid exposure should be achieved by mixing protonated molecules near the crystal surface with non-protonated molecules that remained in the interior of the crystal. The extension of the MCL shift *via* surface protonation of crystals serves as a new method for manipulating the MCL behavior of crystalline materials, which should accelerate the future development of MCL materials with rationally controlled properties.

## Introduction

Solid-state-emissive materials capable of exhibiting mechanochromic luminescence (MCL) have recently attracted a lot of attention, and they are expected to be used in sensing technologies for visualizing mechanical stimuli.[1] A considerable number of donor–acceptor (D–A)-type fluorophores with electron-rich and -deficient substituents or heteroaromatic rings have been developed as crystalline MCL materials that can switch their emission colors by amorphization or phase transition to other polymorphs triggered by mechanical stimuli such as grinding or pressure.[2] The emission wavelength of the D–A-type fluorophores is sensitive to the polarity of the surrounding environments and thus significantly shifts in the bathochromic or hypsochromic direction when the intermolecular interactions between polar D–A molecules are altered by the mechanical-stimuli induced phase transitions.[3] From a practical perspective of MCL materials, the control over the magnitude of the emission-wavelength shift in the MCL is particularly desirable for constructing precise mechano-sensing systems. Nonetheless, despite recent intensive research on MCL compounds, rational control over the MCL shift remains a significant challenge.

Several methods for tuning the MCL shift of organic fluorophores have been developed. The simplest method is to synthesize a new derivative with a different substituent on the parent compound.[4,5] In this approach, the solid-state emission color and MCL shift can be modulated based on the electronic and steric effects of the introduced substituent. However, laborious chemical synthesis is required, and the rational prediction of the substituent effect on the MCL properties remains difficult. Other methods for controlling the MCL shift without changing the molecular structure have been reported, including incidental crystallization of polymorphs

---

[a] *Department of Chemistry and Life Science, Graduate School of Engineering Science, Yokohama National University, 79-5 Tokiwadai, Hodogaya-ku, Yokohama 240-8501, Japan. E-mail: suguru-ito@ynu.ac.jp*

[b] *Department of Chemistry, Graduate School of Science, Kobe University, 1-1 Rokkodai-cho, Nada-ku, Kobe 657-8501, Japan*

[c] *Molecular Photoscience Research Center, Kobe University, 1-1 Rokkodai-cho Nada-ku, Kobe 657-8501, Japan. E-mail: tachikawa@port.kobe-u.ac.jp*

[d] *PRESTO, Japan Science and Technology Agency (JST), 4-1-8 Honcho, Kawaguchi, Saitama 332-0012, Japan*

† Electronic supplementary information (ESI) available: Supplementary spectra, PXRD data, DSC data, theoretical calculations, fluorescence microscopy, and movie of *in situ* fluorescence microscopy. CCDC 2153514 (**1**) and 2153515 (**2**). For ESI and crystallographic data in CIF or other electronic format see DOI: https://doi.org/10.1039/d2ma00256f

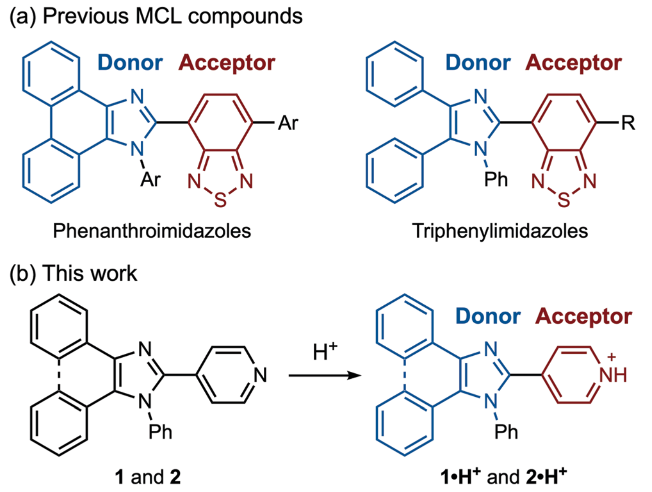

Fig. 1 (a) Structures of previously reported D–A-type MCL compounds. (b) Protonation of pyridyl-substituted imidazole derivatives **1** and **2**.

and pesudopolymorphs.[6,7] The MCL behaviors observed by these methods are attributed to the differences in the conformation and intermolecular interactions of molecules in various crystal structures and amorphous states. Producing cocrystals or two-component dyes by mixing one compound with another is a more convenient way to tune the emission properties of one compound.[8] Their MCL properties can be affected by noncovalent interactions, energy transfer, or charge transfer between the two compounds. Protonation of basic substituents is one of the most common noncovalent interactions used to control the luminescence properties of organic fluorophores.[9] Nevertheless, protonation of fluorophores has received little attention for regulating the MCL properties.[10]

Herein, we demonstrate that the protonation of pyridyl-substituted fluorophores **1** and **2** rationally extends the range of MCL shifts. We have recently reported that D–A-type dyes composed of electron-donating imidazole and electron-accepting benzothiadiazole rings exhibit a wide variety of MCL properties (Fig. 1a).[11] The present strategy takes advantage of the acid-induced enhancement of the electron-accepting property of the pyridyl group attached to phenanthroimidazole or triphenylimidazole groups (Fig. 1b). Compared with the original non-protonated crystals of phenanthroimidazole **1** and triphenylimidazole **2**, the acid-exposed crystals have achieved more distinct MCL shifts owing to the increased D–A character of the fluorophores. Following powder X-ray diffraction (PXRD) analysis, spatially resolved fluorescence microscopy, and fluorescence lifetime analysis, we propose that the extension of MCL shifts has been realized by the mixture of protonated molecules near the crystal surface and non-protonated molecules that remained in the interior of the crystal.

## Results and discussion

### Synthesis and emission properties

Pyridyl-substituted phenanthroimidazole **1** and triphenylimidazole **2** were synthesized by four-component condensation reactions. In the presence of anhydrous sodium sulfate (2.8 equiv.), the mixtures of 9,10-phenanthrenequinone or benzil with ammonium acetate, aniline, and 4-pyridinecarboxaldehyde were refluxed in acetic acid to give **1** and **2** in 86% and 48% yield, respectively (Scheme 1).

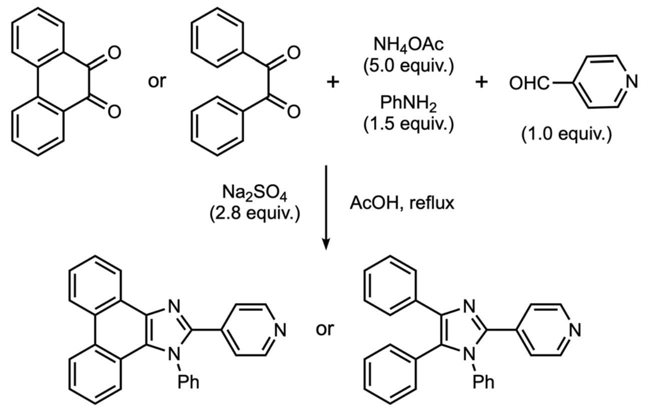

**1** 86% (20 h) **2** 48% (16 h)

Scheme 1 Syntheses of **1** and **2**.

The crystals of **1**, prepared by recrystallization from ethyl acetate, showed MCL capable of switching the maximum emission wavelength of 38 nm (Fig. 2a and c). Under UV irradiation (310 nm), the crystalline samples of **1** exhibited blue-violet emission with a maximum emission wavelength ($\lambda_{\mathrm{em}}$) of 397 nm and an emission quantum yield ($\Phi_{\mathrm{F}}$) of 0.06. Upon grinding crystalline **1** with a spatula, the emission band of **1** was shifted in the bathochromic direction, resulting in blue emission ($\lambda_{\mathrm{em}}$ = 435 nm, $\Phi_{\mathrm{F}}$ = 0.28). When ground **1** was heated at 210 °C, the original emission color was restored.

On the basis of PXRD and differential scanning calorimetry (DSC) analyses, the mechanism for the MCL of **1** should be attributed to the crystal-to-amorphous phase transitions

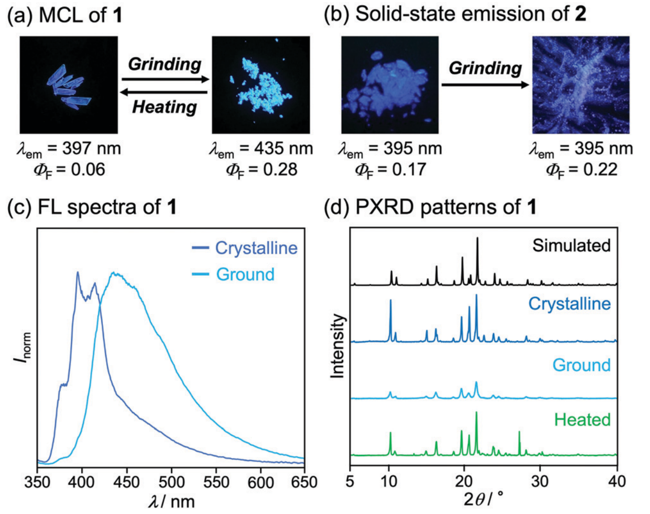
(a) MCL of **1** (b) Solid-state emission of **2**

(c) FL spectra of **1** (d) PXRD patterns of **1**

Fig. 2 Photographs of crystalline and ground (a) **1** and (b) **2** under UV (365 nm) irradiation. (c) Fluorescence spectra of crystalline and ground **1** ($\lambda_{\mathrm{ex}}$ = 310 nm). (d) PXRD patterns of **1**.

(Fig. 2d). The intensity of the PXRD peaks of crystalline **1** substantially decreased in response to mechanical stimuli. Although weak diffraction peaks were still observed, the majority of the crystals should be amorphized after grinding. The intensity of the diffraction peaks was recovered for the blue-violet-emissive samples obtained by heating the ground **1**. The DSC measurement of ground **1** showed a cold-crystallization peak ($T_c$ = 85 °C) from amorphous to crystalline state followed by an endothermic peak that corresponds to the melting point of the initial crystalline **1** ($T_m$ = 233 °C, Fig. S1a, ESI†). Namely, the ground amorphous **1** should be converted to its initial crystalline state upon heating.

Mechanical stimuli did not affect the emission color of crystalline **2** (Fig. 2b and Fig. S2a, ESI†). Blue-violet emission was observed from crystals of **2** obtained by recrystallization from ethyl acetate ($\lambda_{em}$ = 395 nm, $\Phi_F$ = 0.17). Grinding the crystalline samples of **2** resulted in a significant decrease in the intensity of the PXRD pattern (Fig. S5, ESI†). However, the emission color of ground **2** remained bluish violet. The intensity of the diffraction peaks was recovered after heating, and the DSC thermogram of ground **2** showed a cold-crystallization transition peak ($T_c$ = 67 °C) followed by a melting peak ($T_m$ = 217 °C) (Fig. S1b, ESI†). These findings indicate that grinding and heating of **2** cause a phase transition between crystalline and amorphous states without causing changes in emission color.

Single-crystal X-ray diffraction analysis suggested that the difference in the mechanical-stimulus-responsive behavior of **1** and **2** was attributed to intermolecular interactions on their emission properties (Fig. 3). The single-crystal X-ray diffraction analysis was performed on single crystals of **1** and **2**, which were obtained by vapor diffusion of hexane into their chloroform solutions. The simulated PXRD patterns derived from the single-crystal X-ray diffraction structures were in good agreement with those of crystalline samples obtained by recrystallization from ethyl acetate (Fig. 2d and Fig. S5, ESI†). In the crystalline state, the distance between the phenanthroimidazole rings of **1** was 4.288 Å (Fig. 3c and e), which should be far enough away from each other. As a result, crystalline **1** should show monomer-like emissions with vibrational structures. Upon amorphization of the crystalline **1** by grinding, efficient intermolecular interactions should be formed between the phenanthroimidazole rings of adjacent molecules because of the high molecular flexibility and mobility in the amorphous state. The emission wavelength should shift in the bathochromic direction owing to the excited state stabilization. In the crystalline state of **2**, the distance between the imidazole rings of the adjacent molecules was 3.921 Å (Fig. 3d), and the pyridyl and triphenyl groups were in the staggered position (Fig. 3f). Accordingly, the π-conjugation system of **2** should not form effective intermolecular interactions in the crystalline state. Moreover, even in the amorphous state after grinding, the effective intermolecular interactions of **2** should not be formed due to the steric hindrance of the triphenyl group. Therefore, the intermolecular distance in the amorphous state of **2** would be almost the same as that in crystalline **2**, which could explain why crystalline **2** did not respond to mechanical stimuli.

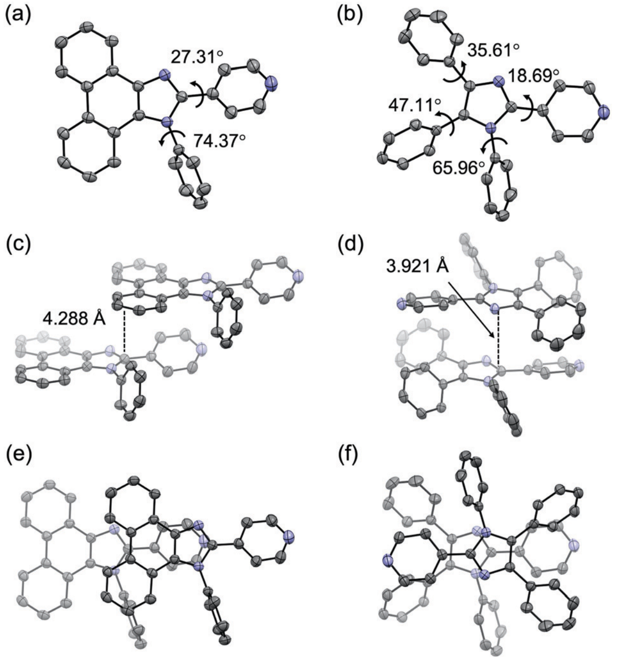

Fig. 3 Molecular structures of (a) **1** and (b) **2** with thermal ellipsoids at 50% probability. (c and d) Side view and (e and f) top view for two adjacent molecules in crystalline **1** (c and e) and **2** (d and f). All hydrogen atoms are omitted for clarity. Color code: gray = C; blue = N.

### Multi-stimuli-responsive behaviors

The MCL shift of **1** increased after being exposed to acid vapor (Fig. 4). When the crystals of **1** were exposed to 6 M HCl vapor for 30 min, the blue-violet emission of **1** was quenched (Fig. 4a). Upon grinding the acid-exposed state, the emission color changed to yellow ($\lambda_{em}$ = 583 nm, $\Phi_F$ = 0.13). Exposure to ethyl acetate vapor changed the yellow-emissive state to a green-emissive state ($\lambda_{em}$ = 519 nm, $\Phi_F$ = 0.06). Grinding the green-emissive state recovers the yellow emission. Namely, the acid-exposed **1** exhibited the MCL with an emission wavelength shift of 64 nm, which was significantly greater than the MCL shift of the pristine **1** ($\Delta\lambda_{em}$ = 38 nm) (Fig. 4b). Upon heating the yellow-emissive state at 210 °C, the original blue-violet emission color was recovered owing to the removal of HCl.

Triphenylimidazole **2** also showed MCL after being treated with HCl vapor (Fig. 5 and Fig. S2b, ESI†). Upon exposure to 6 M HCl vapor for 30 min, the blue-violet emission of the crystalline **2** shifted in the bathochromic direction to show blue emission ($\lambda_{em}$ = 455 nm, $\Phi_F$ = 0.02). In response to grinding stimuli, the emission wavelength of the acid-exposed **2** further shifted bathochromically to show blue-green emission ($\lambda_{em}$ = 496 nm, $\Phi_F$ = 0.04). The blue-green-emissive state changed to a blue-emissive state after being exposed to ethyl acetate vapor ($\lambda_{em}$ = 459 nm, $\Phi_F$ = 0.11), and the blue-green emission was restored by grinding the blue-emissive state. Namely, the acid-exposed **2** exhibited MCL with a maximum emission wavelength shift of 37 nm. The original blue-violet-emissive state was recovered by heating the blue-green-emissive state at 190 °C.

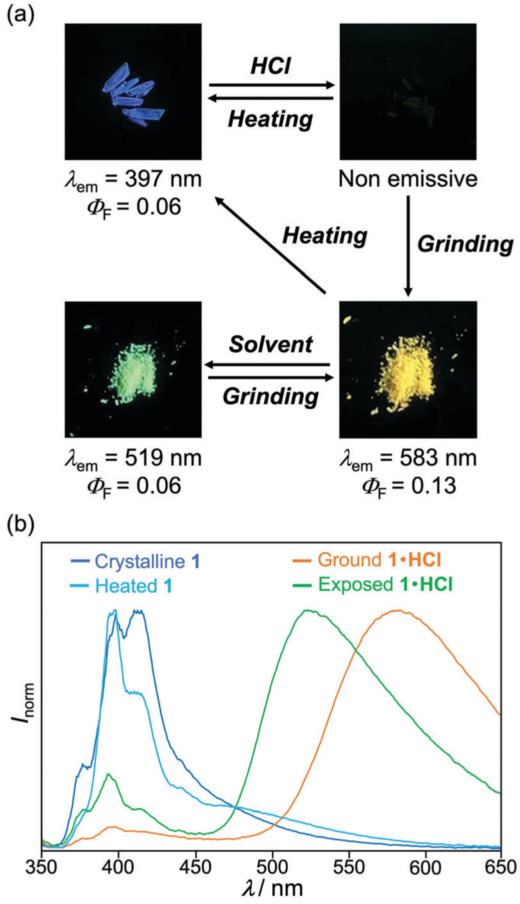

Fig. 4 Photographs of multi-stimuli-responsive emission of (a) **1** under UV (365 nm) irradiation. (b) Fluorescence spectra of crystalline **1**, heated **1**, ground **1·HCl**, and solvent-exposed **1·HCl** ($\lambda_{ex}$ = 310 nm).

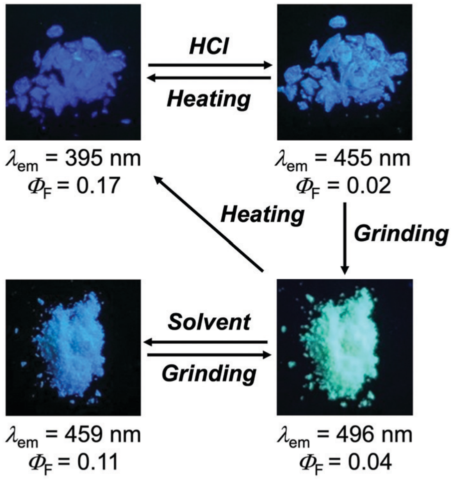

Fig. 5 Photographs of multi-stimuli-responsive emission of **2** under UV (365 nm) irradiation.

## Photophysical properties of protonated compounds

The acid-treated derivatives **1·HCl** and **2·HCl** should exhibit intramolecular charge-transfer emission owing to the protonation of the pyridyl group. The absorption spectrum of **1** in chloroform solution ($1.0 \times 10^{-4}$ M) showed a maximum absorption wavelength ($\lambda_{abs}$) of 333 nm with vibrational structures (Fig. 6a). Under the irradiation with UV light (331 nm), the violet fluorescence ($\lambda_{em}$ = 401 nm, $\Phi_F$ = 0.26) was observed from the chloroform solution ($1.0 \times 10^{-5}$ M) of **1** (Fig. 6c). Meanwhile, after crystalline **1** was sufficiently protonated by exposing to 6 M HCl vapor for 13 h, the $\lambda_{abs}$ of the resulting **1·HCl** in chloroform solution was shifted in the bathochromic direction to 428 nm, exhibiting blue-green fluorescence ($\lambda_{em}$ = 482 nm, $\Phi_F$ = 0.45, Fig. S11a, ESI†).[12] Density functional theory (DFT) calculations of **1** and protonated **1·H$^+$** revealed that the localization of LUMO on the pyridyl group was significantly enhanced in the protonated **1·H$^+$** when compared with the non-protonated **1** (Fig. S7, ESI†). Time-dependent (TD)-DFT calculations of **1** and **1·H$^+$** confirm the experimental finding that the $\lambda_{abs}$ of **1** had shifted in the bathochromic direction upon protonation (calcd. $\lambda_{abs}$: 296.02 nm for **1** and 432.04 nm for **1·H$^+$**, Table S1, ESI†). Similarly, the absorption and fluorescence spectra of **2·HCl** in chloroform solution were observed in the bathochromic regions when compared to those of **2** (Fig. 6d, Fig. S8, and S11b, ESI†), which is supported by the TD-DFT calculations of **2** and **2·H$^+$** (Fig. S7 and Table S1, ESI†). The solid-state absorption spectra of **1·HCl** and **2·HCl** were also observed in bathochromic regions in comparison to those of **1** and **2** (Fig. S10, ESI†).

The absorption and fluorescence spectra of phenanthroimidazole derivative **3** with the 2-phenyl group instead of the 2-pyridyl group of **1** further confirmed that the spectral changes

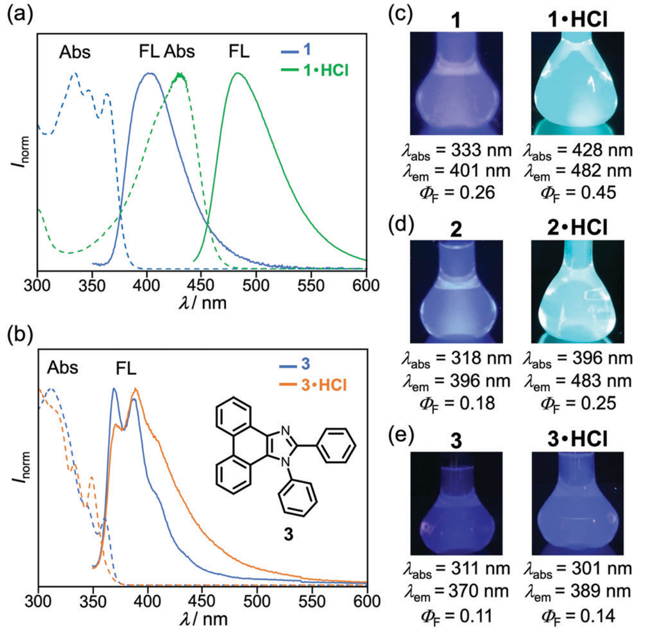

Fig. 6 Absorption (dotted line) and fluorescence (solid line) spectra of (a) **1** and **1·HCl** and (b) **3** and **3·HCl** in chloroform solution [$\lambda_{ex}$ = 331 nm (**1**), 430 nm (**1·HCl**), 313 nm (**3**), and 309 nm (**3·HCl**)]. Photographs of (c) **1** and **1·HCl**, (d) **2** and **2·HCl**, and (e) **3** and **3·HCl** in chloroform solution under UV (365 nm) irradiation.

of **1** and **2** are attributed to the protonation of the pyridyl group. A chloroform solution of **3** ($1.0 \times 10^{-4}$ M) showed a maximum absorption wavelength at 311 nm and violet fluorescence peaking at 370 nm ($\Phi_F = 0.11$) with vibrational structures (Fig. 6b and e). The solution-state spectra of **3** were almost identical to those of **3·HCl** prepared by exposing crystalline **3** to 6 M HCl vapor for 13 h, although the fluorescence spectrum of **3·HCl** showed a slight increase in the emission intensity at the long-wavelength region. These results indicate that protonation of the pyridyl group, rather than the imidazole ring, has a significant impact on the photophysical properties of **1** and **2**.

### Mechanistic studies on the extended MCL *via* fluorescence microscopy

In the quenched state obtained by exposing the crystalline **1** to HCl vapor, only the surface should be protonated. *In situ* fluorescence microscopy of the crystalline **1** during exposure to HCl vapor showed that the fluorescence on the surface of crystals changed from blue to green and was then quenched (Fig. 7). Fluorescence microscopy also revealed that small microcrystals (*ca.* 1–4 μm) attached to the surface of the crystals changed their luminescence more quickly than the surface of the larger crystal (Fig. 7 and Movie S1, ESI†). Since such smaller microcrystals have large surface areas, the rapid change in emission color upon exposure to acid should be explained by a rapid increase in the proportion of protonated **1** to the total molecules that comprise the microcrystals.

When the acid-exposed crystals of **1** were gently crushed with a spatula, the resulting powder exhibited a broad emission spectrum (Fig. 8a and b). The concentration quenching of luminescence for the acid-exposed crystals should be caused by strong surface–dipole interactions[13] between polar protonated molecules on the crystal surface. Meanwhile, mixing the protonated and non-protonated **1** by crushing should suppress such concentration quenching, resulting in the broad emission spectrum being observed. Although the maximum emission wavelength was 459 nm, vibrational peaks that correspond to the luminescence from crystalline **1** were observed at around 400 nm. In addition, the PXRD analysis indicated that the crystallinity remained in the crushed **1·HCl** (Fig. 8c). These results imply that the protonation by acid occurred only near the surface of crystals (Fig. 9a and b) and that the broad emission spectrum of the crushed sample should be attributed to a mixture of **1·HCl** on the crystal surface and non-protonated **1** in the interior of the crystal.

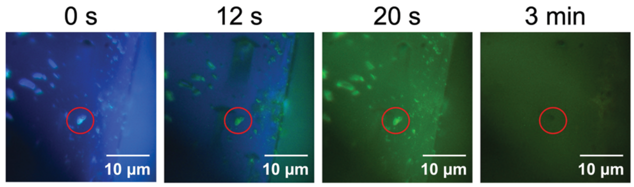

Fig. 7 Emission images of crystalline **1** during exposure to acid recorded by fluorescence microscopy ($\lambda_{ex}$ = 405 nm). The red circles indicate a microcrystal attached to the surface of a large crystal.

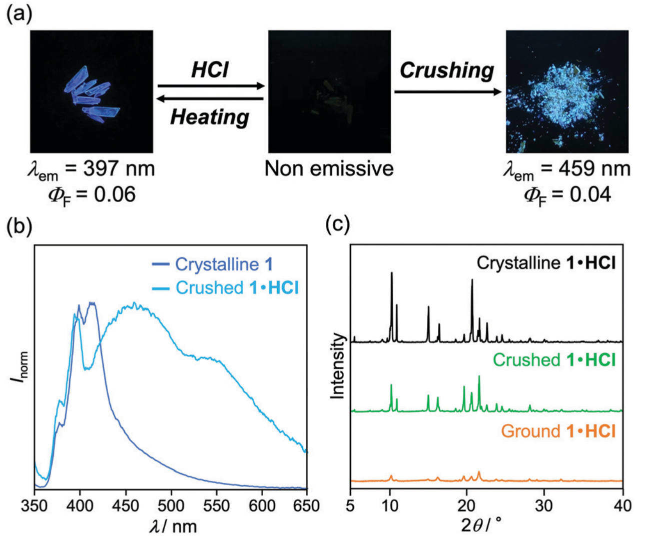

Fig. 8 (a) Photographs of **1**, **1·HCl**, and crushed **1·HCl** under UV (365 nm) irradiation. (b) Fluorescence spectra of crystalline **1** and crushed **1·HCl** ($\lambda_{ex}$ = 310 nm). (c) PXRD patterns of crystalline, crushed, and ground **1·HCl**.

Fluorescence microscopy of the crushed **1·HCl** revealed that the crushed **1·HCl** contains blue-, green-, and yellow-green-emissive states **1·HCl-B**, **1·HCl-G**, and **1·HCl-YG** (Fig. 10). The blue emission of **1·HCl-B** should be assignable to the luminescence from amorphous **1**, which is generated from the internal crystalline **1** upon crushing the surface-protonated crystals. Moreover, since the emission color of crystalline **1** initially changed from blue to green upon protonation (Fig. 7), the green emission of **1·HCl-G** should be rationalized by the luminescence from partially protonated crystals of **1**. Meanwhile, the **1·HCl-YG** state should be an amorphous mixture of **1** and **1·HCl**.

The fluorescence lifetimes of **1·HCl-B**, **1·HCl-G**, and **1·HCl-YG** were analyzed by the fluorescence decay profiles (Table 1 and Fig. S12a, ESI†). The blue emission of **1·HCl-B** was composed of two luminescent components with fluorescence lifetimes of 0.8 ns ($\tau_1$) and 3.9 ns ($\tau_2$), respectively. On the other hand, the green-emissive **1·HCl-G** contained two components with relatively shorter lifetimes ($\tau_1$ = 0.3 ns, $\tau_2$ = 3.0 ns). Although two components with similar lifetimes were found in the yellow-green-emissive **1·HCl-YG** ($\tau_1$ = 0.4 ns, $\tau_2$ = 2.4 ns), the third component with the longest lifetime ($\tau_3$ = 11.9 ns) was dominant.

The yellow-emissive ground state of **1·HCl** contained a relatively long-lived emission component ($\tau_3$ = 10.5 ns, Table 2, Fig. S12b and S13, ESI†) that was nearly identical to the emission component observed in the crushed **1·HCl-YG**. The PXRD analysis confirmed that grinding the crushed **1·HCl** reduced the intensity of the diffraction peaks (Fig. 8c). These results support the hypothesis that the yellow fluorescence is emitted from an amorphous state composed of a mixture of protonated **1·HCl** and non-protonated **1** (Fig. 9c). When the ground **1·HCl** was mixed with non-protonated **1**, the emission band was gradually shifted in the hypsochromic direction with a progressive increase in the amount of **1** (Fig. S4, ESI†). Since the intensity of the yellow

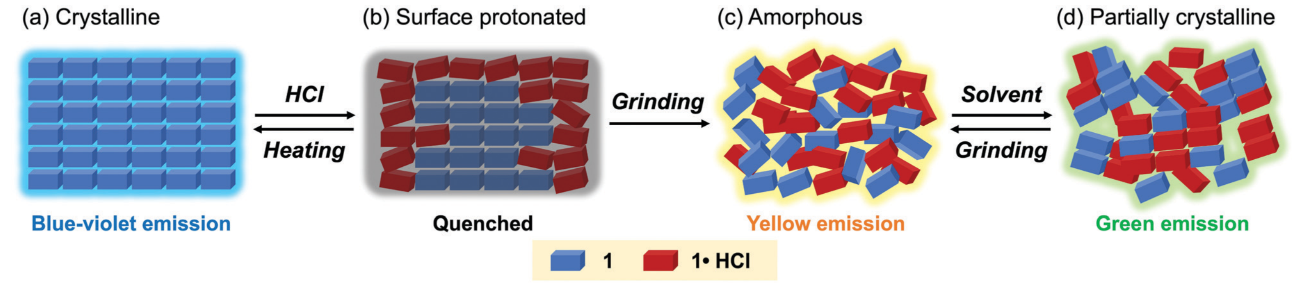

Fig. 9 Schematic illustration of molecular arrangements. (a) Cross-sectional view of an initial crystalline **1**. (b) Cross-sectional view of a surface-protonated crystal of **1** after exposure to HCl vapor. (c) Amorphous mixture of **1** and **1·HCl** after grinding the surface protonated crystal. (d) Partially crystalline mixture of **1** and **1·HCl** after exposing solvent vapor to the amorphous mixture.

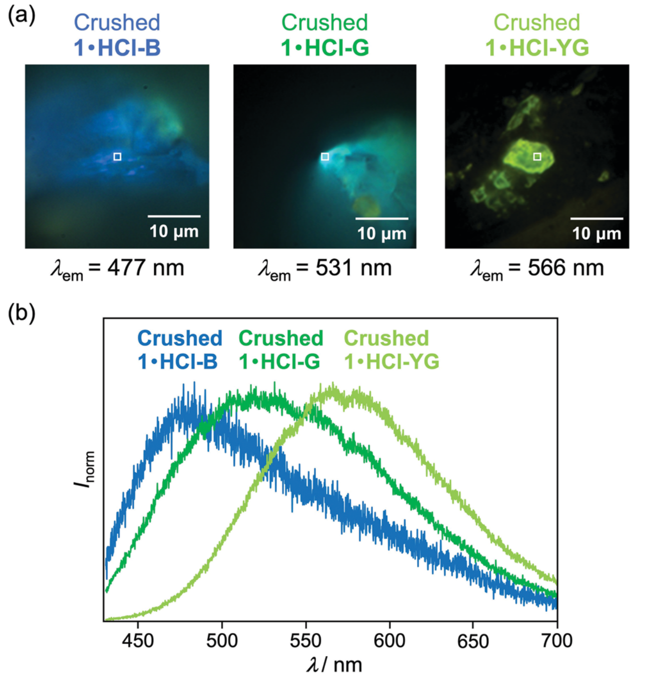

Fig. 10 (a) Photographs and (b) fluorescence spectra of crushed **1·HCl-B**, **1·HCl-G**, and **1·HCl-YG** recorded by fluorescence microscopy ($\lambda_{ex}$ = 405 nm). The square marks indicate the measured locations of the fluorescence spectra and fluorescence decay profiles.

Table 1 Maximum emission wavelength and fluorescence lifetimes of **1·HCl-B**, **1·HCl-G**, and **1·HCl-YG** observed in the crushed **1·HCl**

| State | $\lambda_{em}{}^{a}$ (nm) | $\tau_1{}^{b}$ (ns) | $\tau_2{}^{b}$ (ns) | $\tau_3{}^{b}$ (ns) | $\langle\tau\rangle^{c}$ (ns) |
|---|---|---|---|---|---|
| **1·HCl-B** | 477 | 0.8 (0.49) | 3.9 (0.51) | — | 2.4 |
| **1·HCl-G** | 531 | 0.3 (0.27) | 3.0 (0.73) | — | 2.3 |
| **1·HCl-YG** | 566 | 0.4 (0.04) | 2.4 (0.25) | 11.9 (0.71) | 9.1 |

[a] The maximum emission wavelength observed by fluorescence microscopy ($\lambda_{ex}$ = 405 nm). [b] The fractional contribution $f_n$ of the component is indicated in parentheses. [c] Intensity-weighted mean fluorescence lifetime. $\langle\tau\rangle = f_1\tau_1 + f_2\tau_2 + f_3\tau_3$.

Table 2 Maximum wavelength and lifetime of ground and exposed **1·HCl**

| Sample | $\lambda_{em}{}^{a}$ (nm) | $\tau_1{}^{b}$ (ns) | $\tau_2{}^{b}$ (ns) | $\tau_3{}^{b}$ (ns) | $\langle\tau\rangle^{c}$ (ns) |
|---|---|---|---|---|---|
| Ground **1·HCl** | 588 | 0.3 (0.02) | 2.0 (0.20) | 10.5 (0.78) | 8.6 |
| Exposed **1·HCl** | 529 | 1.4 (0.19) | 7.2 (0.81) | — | 6.1 |

[a] The maximum emission wavelength observed by fluorescence microscopy ($\lambda_{ex}$ = 405 nm). [b] The fractional contribution $f_n$ of the component is indicated in parentheses. [c] Intensity-weighted mean fluorescence lifetime. $\langle\tau\rangle = f_1\tau_1 + f_2\tau_2 + f_3\tau_3$.

emission from the ground **1·HCl** was not decreased after mixing with **1**, the yellow emission would not be attributed to exciplexes between **1** and **1·HCl**. The excited state of **1·HCl** would be simply stabilized by the surrounding polar molecules in the ground amorphous state, which should explain the observed yellow emission.

Partial crystallization from the yellow-emissive amorphous state accounts for the emission-color change caused by solvent vapor exposure (Fig. 9d). The PXRD analysis indicated that the intensity of the diffraction peaks was partially recovered after exposure to ethyl acetate vapor (Fig. S6, ESI†). Because this crystallization occurred from the amorphous mixture **1** and **1·HCl**, the solvent-exposed **1·HCl** showed the new green emission rather than the original blue emission. In the exposed **1·HCl**, two fluorescence components ($\tau_1$ = 1.4 ns, $\tau_2$ = 7.2 ns) with shorter lifetimes than ground **1·HCl** were observed (Table 2, Fig. S12b and S13, ESI†). Such emissive components were not found in the crushed **1·HCl**, indicating that the partially crystallized state with green luminescence is different from parts of the surface protonated state. The decrease in fluorescence lifetimes would be attributed to a change in intermolecular interactions caused by crystallization, which should reduce the stabilizing effects of the excited molecules. Accordingly, the emission wavelength from the mixture of **1** and **1·HCl** should be shifted in the hypsochromic direction by partial crystallization from the amorphous state.

The improvement in MCL shift upon exposure to acid should be rationalized by the increased polarity of **1** after being protonated at the pyridyl groups. Since the emission wavelength of the protonated forms should be more sensitive to the polarity of surroundings, the mixture of protonated **1·HCl** and non-protonated **1** should show larger shifts in the emission band when the polar environment based on intermolecular interactions is changed between crystalline and amorphous states.

As discussed for **1**, the surface protonation of crystals should account for the mechanism of the extended MCL shift in **2**. Upon gently crushing a blue-emissive crystal of **2·HCl**, the resulting powder showed blue-violet luminescence, which should be derived from non-protonated **2** (Fig. S3, ESI†). The crushed crystalline **2·HCl** was changed to the blue-green-emissive amorphous state after grinding (Fig. S5, ESI†). The subsequent emission-color change of the ground **2·HCl** by exposing ethyl acetate vapor was attributed to partial recrystallization from the amorphous state. Although non-protonated **2** did not exhibit MCL, the significant MCL shift of protonated **2** should be explained by the increased D–A properties upon protonation. The protonated molecules are sensitive to the surrounding polarity change, and therefore the emission color of the mixture of **2** and **2·HCl** changed even by a subtle difference in intermolecular interactions between crystalline and amorphous states. Moreover, the smaller MCL shift of protonated **2** compared with that of protonated **1** would be explained by the steric hindrance of the phenyl groups in **2**, which should suppress the intermolecular interactions of **2** and **2·HCl**.

## Conclusions

In summary, the MCL shifts of pyridyl-substituted imidazole derivatives **1** and **2** could be extended after being exposed to HCl vapors. The pristine crystals of **1** showed MCL between blue-violet and blue, with the MCL shift of 38 nm. Upon exposure to acid, the range of wavelength shift increased to 64 nm, causing the emission color to alternate between green and yellow. The crystalline state of **2** exhibited blue-violet emission and the luminescence did not change in response to mechanical stimuli. The emission color of **2** changed to blue by exposure to acid and to blue-green by subsequent grinding. This blue-green-emissive state showed MCL with an emission shift of 37 nm. *In situ* fluorescence microscopy of the protonation process revealed that microcrystals with large surface areas were rapidly changed to a non-emissive state when compared to the larger crystal. The PXRD analysis and spatially resolved fluorescence microscopy of the crushed **1·HCl** revealed that the crushed sample is a mixture of protonated **1·HCl** near the crystal surface and non-protonated **1** that remained in the interior of the crystal. The extended MCL shifts for the mixtures of protonated and non-protonated **1** and **2** should be rationalized by the increased polarity of the protonated fluorophores. This study sheds light on the development of new strategies for creating novel MCL dyes with desirable emission-color shifting properties.

## Experimental

### General

All air-sensitive experiments were carried out under an argon atmosphere unless otherwise noted. Silica gel 60 N (spherical, neutral, 63–210 μm) was used for column chromatography. 1,2-Diphenyl-1*H*-phenanthro[9,10-*d*]imidazole (**3**) was synthesized according to the literature procedure.[14] Other reagents and solvents were commercially available and were used as received. $^1$H and $^{13}$C NMR spectra were recorded on a JEOL ECA-500 spectrometer using tetramethylsilane as an internal standard. A miniature fiber-optic spectrometer (FLAME-S-XR1-ES, Ocean Optics) and a LED light (310 nm, LSM-310A, Ocean Optics) were used for the measurements of fluorescence spectra of stimuli-responsive luminescence. Fluorescence and UV-vis absorption spectra were measured on a JASCO FP-8300 fluorescence spectrometer. The absolute fluorescence quantum yields ($\Phi_F$) were determined using a 100 mm $\phi$ integrating sphere JASCO ILF-835. A KBr plate sample holder was used for the measurement of $\Phi_F$ to set a powdered sample between two KBr plates (5 × 5 × 1 mm). The solid-state absorption spectra were obtained by measuring diffuse reflectance spectra using an FPA-810 powder sample cell block. For the measurement of UV-vis absorption spectra in chloroform, an FUV-803 absorbance measurement cell block was used. PXRD measurements were performed on a Rigaku SmartLab system using CuKα radiation. Melting points were determined on a Stuart melting point apparatus SMP3 and are uncorrected. DSC data were recorded on a Shimadzu DSC-60 plus (heating rate: 10 °C min$^{-1}$). High-resolution mass spectra (HRMS-ESI) were recorded on a Hitachi Nano Frontier LD spectrometer.

### Preparation of pyridyl-substituted imidazole derivatives

**Synthesis of 1-phenyl-2-(pyridin-4-yl)-1*H*-phenanthro[9,10-*d*]-imidazole (1)[15].** To a stirred solution of 4-pyridinecarboxaldehyde (1.0 mmol, 0.10 mL), aniline (1.5 mmol, 0.14 mL), and anhydrous sodium sulfate (2.8 mmol, 0.395 g) in acetic acid (6.0 mL) were added 9,10-phenanthrenequinone (1.0 mmol, 0.208 g) and ammonium acetate (5.2 mmol, 0.397 g). After the mixture was stirred for 20 h at 120 °C, a saturated aqueous solution of $NaHCO_3$ and dichloromethane were added to the mixture. The organic layer was separated, and the aqueous layer was extracted three times with dichloromethane. The combined organic layer was washed with water and brine, dried over anhydrous $Na_2SO_4$, and filtered. After removal of the solvent under reduced pressure, the crude product was purified by column chromatography on silica gel (dichloromethane/ethyl acetate = 1 : 3) to give 1-phenyl-2-(pyridin-4-yl)-1*H*-phenanthro-[9,10-*d*]imidazole (**1**, 0.318 g, 86%) as a pale yellow solid. The purified product was dissolved in hot ethyl acetate (17 mL, 75 °C), and the solution was cooled to room temperature to give pale yellow crystals.

M.p. 232.7–233.9 °C, IR (KBr): $\nu_{max}$ 3029, 1598, 1497, 1451, 1411, 1385, 1069, 992, 869, 825, 810, 758 cm$^{-1}$; $^1$H NMR (500 MHz, $CDCl_3$): $\delta$ (ppm) 8.85 (dd, *J* = 8.0, 1.1 Hz, 1H), 8.76 (d, *J* = 8.3 Hz, 1H), 8.69 (d, *J* = 8.3 Hz, 1H), 8.53–8.52 (m, 2H), 7.77–7.64 (m, 5H), 7.55–7.51 (m, 3H), 7.46–7.45 (m, 2H), 7.28–7.25 (m, 1H), 7.16 (d, *J* = 7.4 Hz, 1H); $^{13}$C NMR (126 MHz, $CDCl_3$): $\delta$ (ppm) 149.8 (2C), 147.5, 138.2, 137.8, 137.7, 130.5 (2C), 130.4, 129.6, 128.9, 128.8 (2C), 128.4, 127.4, 127.0, 126.4, 126.0, 125.4, 124.1, 123.1, 122.7 (3C), 122.7, 120.9; HRMS-ESI (*m*/*z*): [M+ H]$^+$ calcd for $C_{26}H_{18}N_3$, 372.1501; found, 372.1507.

**Synthesis of 4-(1,4,5-triphenyl-1*H*-imidazol-2-yl)pyridine (2)[16].** According to the same procedure used for the synthesis of **1**, 4-(1,4,5-triphenyl-1*H*-imidazol-2-yl)pyridine (**2**) was synthesized from benzil, 4-pyridinecarboxaldehyde, aniline, and ammonium acetate in 48% yield as a white solid. The purified product was dissolved in hot ethyl acetate (70 °C), and the solution was cooled to room temperature to give colorless crystals.

M.p. 215.7–216.2 °C, IR (KBr): $\nu_{\max}$ 3036, 1596, 1495, 1420, 1071, 962, 828, 795, 764 cm$^{-1}$; $^1$H NMR (500 MHz, CDCl$_3$): $\delta$ (ppm) 8.48–8.47 (m, 2H), 7.60–7.58 (m, 2H), 7.38–7.30 (m, 5H), 7.28–7.20 (m, 6H), 7.15–7.12 (m, 2H), 7.11–7.04 (m, 2H); $^{13}$C NMR (126 MHz, CDCl$_3$): $\delta$ (ppm) 149.7 (2C), 143.8, 139.1, 137.7, 136.6, 133.9, 132.4, 131.0 (2C), 130.0, 129.4 (2C) 129.0, 128.4 (2C), 128.3, 128.2 (4C), 127.3 (2C), 126.9, 122.3 (2C); HRMS-ESI (*m*/*z*): [M + H]$^+$ calcd for $C_{26}H_{20}N_3$, 374.1657; found, 374.1655.

## X-Ray crystallography

A single crystal of **1** and **2** was obtained from vapor diffusion of hexane into a chloroform solution of the compound. The crystalline samples were mounted on a glass fiber. All measurements were made on a Rigaku XtaLAB P200 diffractometer using multi-layer mirror monochromated Cu-Kα radiation ($\lambda$ = 1.54184 Å). The data were collected at a temperature of −50 ± 1 °C. The crystal-to-detector distance was 40.00 mm. The readout was performed in the 0.172 mm pixel mode. Data were collected and processed using CrysAlisPro (Rigaku Oxford Diffraction).[17] An empirical absorption correction was applied. The data were corrected for Lorentz and polarization effects. The structure was solved by direct methods (SIR92)[18] and expanded using Fourier techniques. The non-hydrogen atoms were refined anisotropically. Hydrogen atoms were refined using the riding model. All calculations were performed using the CrystalStructure[19] crystallographic software package except for refinement, which was performed using SHELXL Version 2014/7.[20]

Crystal data for **1** (CCDC2153514): $C_{26}H_{17}N_3$, $M$ = 371.44, orthorhombic, $a$ = 17.1153(3) Å, $b$ = 32.2108(5) Å, $c$ = 6.80561(12) Å, $V$ = 3751.91(11) Å$^3$, space group *Aea*2 (no. 41), $Z$ = 8, $D_c$ = 1.315 g cm$^{-3}$, $F$(000) = 1552.00, $T$ = 223(1) K, $\mu$(Cu-Kα) = 6.117 cm$^{-1}$, 7009 reflections measured, 2796 independent ($R_{\text{int}}$ = 0.0407). The final refinement converged to $R_1$ = 0.0493 for $I > 2.0\sigma(I)$, w$R_2$ = 0.1260 for all data.

Crystal data for **2** (CCDC2153515): $C_{26}H_{19}N_3$, $M$ = 373.46, monoclinic, $a$ = 21.1994(2) Å, $b$ = 8.13989(8) Å, $c$ = 24.4484(3) Å, $b$ = 113.4124(13)°, $V$ = 3871.49(8) Å$^3$, space group *I*2/*a* (no. 15), $Z$ = 8, $D_c$ = 1.281 g cm$^{-3}$, $F$(000) = 1568.00, $T$ = 223(1) K, $\mu$(Cu-Kα) = 5.931 cm$^{-1}$, 11363 reflections measured, 3533 independent ($R_{\text{int}}$ = 0.0274). The final refinement converged to $R_1$ = 0.0402 for $I > 2.0\sigma(I)$, w$R_2$ = 0.1041 for all data.

## Measurement of stimuli-responsive emission

**Typical experimental procedure for the measurement of the MCL.** Crystalline samples of **1** on an agate mortar were manually ground by using an agate pestle. The emission spectrum of the ground sample was measured using a miniature fiber-optic spectrometer. The ground sample placed on a slide glass was heated on a hot plate at 210 °C. After the heated sample was cooled to room temperature, the emission spectrum of the sample was measured using a miniature fiber-optic spectrometer.

## Typical experimental procedure for the treatment of HCl and organic solvent vapors

Crystalline samples of **1** (*ca.* 5 mg) on a slide glass was placed in a Petri dish (O.D. × height: 100 mm × 15 mm). In the same Petri dish, 6 M HCl or organic solvent (*ca.* 3 mL) in another Petri dish (O.D. × height: 40 mm × 10 mm) was placed. The larger Petri dish was covered with a lid. After standing for 30 min at room temperature, the change in emission spectrum was observed using a miniature fiber-optic spectrometer.

## Typical experimental procedure for the preparation of $CHCl_3$ solutions for measuring photophysical properties in solution

**Preparation of a $CHCl_3$ solution of 1.** A 5.0 mM $CHCl_3$ solution of **1** was prepared in a 10 mL volumetric flask by dissolving **1** (18.8 mg, 0.05 mmol) into $CHCl_3$. A 1.0 × 10$^{-5}$ M $CHCl_3$ solution of **1** was prepared in a 5 mL volumetric flask by dilution of a 5.0 mM $CHCl_3$ solution of **1** (10 μL) with $CHCl_3$.

**Preparation of a $CHCl_3$ solution of 1·HCl.** Crystalline **1** (18.8 mg, 0.05 mmol) on a glass slide and 6 M HCl (*ca.* 4 mL) in a small Petri dish (O.D. × height: 40 mm × 10 mm) were placed in a large Petri dish (O.D. × height: 100 mm × 15 mm). The larger Petri dish was covered with a lid and allowed to stand at room temperature for 13 h. A 5.0 mM $CHCl_3$ solution of **1·HCl** was prepared in a 10 mL volumetric flask by dissolving all of the exposed **1·HCl**. A 1.0 × 10$^{-5}$ M $CHCl_3$ solution of **1·HCl** was prepared in a 5 mL volumetric flask by dilution of 5.0 mM $CHCl_3$ solution of **1·HCl** (10 μL) with $CHCl_3$.

## Theoretical calculations

The theoretical calculations were performed using the Gaussian 16 program.[21] Optimization of the molecular structures of **1** and **2** was carried out by DFT calculations at the CAM-B3LYP/6-31G(d) level of theory, using the single-crystal X-ray diffraction structures as the initial geometry. The six lowest singlet–singlet transitions of the optimized structure of **1** and **2** were calculated using TD-DFT calculations at the CAM-B3LYP/6-31G(d) level of theory. Here, the long-range-corrected hybrid functional CAM-B3LYP was used, as CAM-B3LYP often provides better results in TD-DFT calculations than B3LYP, which is conventionally used in DFT calculations.[22] Optimization of the protonated **1·H$^+$** and **2·H$^+$** of the optimized **1** and **2** was also carried out by DFT calculations at the same level of theory. The six lowest singlet–singlet transitions of the optimized **1·H$^+$** and **2·H$^+$** were calculated using TD-DFT calculations at the same level of theory. The results of the theoretical calculations are presented in Table S1 (ESI†).

## Fluorescence microscopy

The crystals were dispersed on a clean cover glass (Matsunami Glass). The cover glass was transferred to an imaging chamber (Attofluor cell chamber, Invitrogen), which was mounted onto a microscope stage. Immediately after dropping a small amount of concentrated HCl solution (35.0–37.0%, Wako) on the edge of the cover glass, the chamber was covered with a glass plate for *in situ* observation of the protonation process. Spatially resolved fluorescence measurements were performed on a home-built wide-field/confocal microscope equipped with a Nikon Ti-E inverted fluorescence microscope. The fluorescence images were recorded using a color sCMOS camera (Dhyana 400DC, Tucsen Photonics). The 405 nm continuous wave laser (OBIS 405LX, Coherent) or 405 nm pulsed diode laser (PiL040X, Advanced Laser Diode System, 45 ps FWHM) was used to excite the samples. A dichroic mirror (Di02-R405, Semrock) and a longpass filter (ET425lp, Chroma) were used to filter the scattering from the excitation light. An area of approximately 1 μm$^2$ on a target particle or region was spatially selected using a 100 μm pinhole to measure its spectrum and fluorescence lifetime. For the spectroscopy, only the emission that passed through the pinhole and a slit entered the imaging spectrograph (MS3504i, SOL instruments) equipped with a CCD camera (DU416A-LDC-DD, Andor). For time-resolved fluorescence measurements, the emitted photons were passed through the pinhole and then directed onto a single-photon avalanche diode (SPD-050, Micro Photon Devices). The signals from the detector were sent to a time-correlated single photon counting module (SPC-130EM, Becker & Hickl) for further analysis. The instrument response function of the system was about 100 ps. All the experiments were conducted at room temperature. The data were analyzed using ImageJ (**https://rsb.info.nih.gov/ij/**) and Origin 2021 (OriginLab).

## Author contributions

Rikuto Kubota: investigation, validation, visualization, writing – original draft. Yanqiu Yuan: investigation, writing – review & editing. Ryohei Yoshida: investigation, validation, writing – review & editing. Takashi Tachikawa: conceptualization, funding acquisition, investigation, validation, writing – review & editing. Suguru Ito: conceptualization, funding acquisition, project administration, visualization, writing – review & editing.

## Conflicts of interest

There are no conflicts to declare.

## Acknowledgements

This work was partly supported by JSPS KAKENHI Grant Number JP20K05645 within a Grant-in-Aid for Scientific Research (C), JSPS KAKENHI Grant Numbers JP20H04665 and JP20H04673 within a Grant-in-Aid for Scientific Research on Innovative Areas ("Soft Crystals: Area No. 2903"), and JST, PRESTO Grant Number JPMJPR21A3, Japan. Part of this work was carried out by the joint research program No. R03007 of Molecular Photoscience Research Center, Kobe University.

## Notes and references

1 For reviews, see: (*a*) S. Ito, *J. Photochem. Photobiol., C*, 2022, **51**, 100481; (*b*) T. Mutai and S. Takamizawa, *J. Photochem. Photobiol., C*, 2022, **51**, 100479; (*c*) M. Jin and H. Ito, *J. Photochem. Photobiol., C*, 2022, **51**, 100478; (*d*) S. Ito, *Chem. Lett.*, 2021, **50**, 649; (*e*) M. Kato, H. Ito, M. Hasegawa and K. Ishii, *Chem. – Eur. J.*, 2019, **25**, 5105; (*f*) C. Wang and Z. Li, *Mater. Chem. Front.*, 2017, **1**, 2174; (*g*) Y. Sagara, S. Yamane, M. Mitani, C. Weder and T. Kato, *Adv. Mater.*, 2016, **28**, 1073; (*h*) Z. Ma, Z. Wang, M. Teng, Z. Xu and X. Jia, *ChemPhysChem*, 2015, **16**, 1811.

2 For seminal examples, see: (*a*) Z. Xie, C. Chen, S. Xu, J. Li, Y. Zhang, S. Liu, J. Xu and Z. Chi, *Angew. Chem., Int. Ed.*, 2015, **54**, 7181; (*b*) Y. Lei, Y. Liu, Y. Guo, J. Chen, X. Huang, W. Gao, L. Qian, H. Wu, M. Liu and Y. Cheng, *J. Phys. Chem. C*, 2015, **119**, 23138; (*c*) Z.-H. Guo, Z.-X. Jin, J.-Y. Wang and J. Pei, *Chem. Commun.*, 2014, **50**, 6088; (*d*) J. Sun, X. Lv, P. Wang, Y. Zhang, Y. Dai, Q. Wu, M. Ouyang and C. Zhang, *J. Mater. Chem. C*, 2014, **2**, 5365; (*e*) Y. Ooyama and Y. Harima, *J. Mater. Chem.*, 2011, **21**, 8372; (*f*) Y. Ooyama, Y. Kagawa, H. Fukuoka, G. Ito and Y. Harima, *Eur. J. Org. Chem.*, 2009, 5321.

3 (*a*) S. Ito, T. Taguchi, T. Yamada, T. Ubukata, Y. Yamaguchi and M. Asami, *RSC Adv.*, 2017, **7**, 16953; (*b*) S. Ito, T. Yamada, T. Taguchi, Y. Yamaguchi and M. Asami, *Chem. – Asian J.*, 2016, **11**, 1963.

4 For a review, see: X. Huang, L. Qian, Y. Zhou, M. Liu, Y. Cheng and H. Wu, *J. Mater. Chem. C*, 2018, **6**, 5075.

5 For seminal examples, see: (*a*) J. Wu, Y. Cheng, J. Lan, D. Wu, S. Qian, L. Yan, Z. He, X. Li, K. Wang, B. Zou and J. You, *J. Am. Chem. Soc.*, 2016, **138**, 12803; (*b*) T. Seki, Y. Takamatsu and H. Ito, *J. Am. Chem. Soc.*, 2016, **138**, 6252; (*c*) S. Xue, X. Qiu, Q. Sun and W. Yang, *J. Mater. Chem. C*, 2016, **4**, 1568; (*d*) X. Y. Shen, Y. J. Wang, E. Zhao, W. Z. Yuan, Y. Liu, P. Lu, A. Qin, Y. Ma, J. Z. Sun and B. Z. Tang, *J. Phys. Chem. C*, 2013, **117**, 7334; (*e*) X. Zhang, Z. Chi, B. Xu, C. Chen, X. Zhou, Y. Zhang, S. Liu and J. Xu, *J. Mater. Chem.*, 2012, **22**, 18505; (*f*) X. Zhang, Z. Chi, B. Xu, L. Jiang, X. Zhou, Y. Zhang, S. Liu and J. Xu, *Chem. Commun.*, 2012, **48**, 10895; (*g*) N. D. Nguyen, G. Zhang, J. Lu, A. E. Sherman and C. L. Fraser, *J. Mater. Chem.*, 2011, **21**, 8409.

6 For a review, see: S. Ito, *CrystEngComm*, 2022, **24**, 1112.

7 For seminal examples, see: (*a*) K. Zheng, F. Ni, Z. Chen, C. Zhong and C. Yang, *Angew. Chem., Int. Ed.*, 2020, **59**, 9972; (*b*) T. Seki, K. Kobayashi, T. Mashimo and H. Ito, *Chem. Commun.*, 2018, **54**, 11136; (*c*) M. Okazaki, Y. Takeda, P. Data, P. Pander, H. Higginbotham, A. P. Monkman and S. Minakata, *Chem. Sci.*, 2017, **8**, 2677; (*d*) Y. Matsunaga and J.-S. Yang, *Angew. Chem., Int. Ed.*, 2015, **54**, 7985; (*e*) Z. He, L. Zhang, J. Mei, T. Zhang, J. W. Y. Lam, Z. Shuai, Y. Q. Dong and B. Z. Tang, *Chem. Mater.*, 2015, **27**, 6601; (*f*) T. Seki, T. Ozaki, T. Okura, K. Asakura, A. Sakon, H. Uekusa and H. Ito, *Chem. Sci.*, 2015, **6**, 2187; (*g*) R. Li, S. Xiao, Y. Li, Q. Lin, R. Zhang, J. Zhao, C. Yang, K. Zou, D. Li and T. Yi, *Chem. Sci.*, 2014, **5**, 3922; (*h*) G. R. Krishna, M. S. R. N. Kiran,

C. L. Fraser, U. Ramamurty and C. M. Reddy, *Adv. Funct. Mater.*, 2013, **23**, 1422; (*i*) X. Luo, W. Zhao, J. Shi, C. Li, Z. Liu, Z. Bo, Y. Q. Dong and B. Z. Tang, *J. Phys. Chem. C*, 2012, **116**, 21967.

8 (*a*) S. Ito, R. Sekine, M. Munakata, M. Yamashita and T. Tachikawa, *Chem. – Eur. J.*, 2021, **27**, 13982; (*b*) Z. Wang, F. Yu, W. Chen, J. Wang, J. Liu, C. Yao, J. Zhao, H. Dong, W. Hu and Q. Zhang, *Angew. Chem., Int. Ed.*, 2020, **59**, 17580; (*c*) M. Ikeya, G. Katada and S. Ito, *Chem. Commun.*, 2019, **55**, 12296; (*d*) S. Ito, G. Katada, T. Taguchi, I. Kawamura, T. Ubukata and M. Asami, *CrystEngComm*, 2019, **21**, 53; (*e*) Z. Ma, Y. Ji, Z. Wang, G. Kuang and X. Jia, *J. Mater. Chem. C*, 2016, **4**, 10914; (*f*) H.-J. Kim, D. R. Whang, J. Gierschner, C. H. Lee and S. Y. Park, *Angew. Chem., Int. Ed.*, 2015, **54**, 4330; (*g*) G. Fan and D. Yan, *Sci. Rep.*, 2014, **4**, 4933; (*h*) D. Yan, H. Yang, Q. Meng, H. Lin and M. Wei, *Adv. Funct. Mater.*, 2014, **24**, 587.

9 (*a*) W. Yang, Y. Yang, Y. Qiu, X. Cao, Z. Huang, S. Gong and C. Yang, *Mater. Chem. Front.*, 2020, **4**, 2047; (*b*) B. Shao, R. Jin, A. Li, Y. Liu, B. Li, S. Xu, W. Xu, B. Xu and W. Tian, *J. Mater. Chem. C*, 2019, **7**, 3263; (*c*) F. Wang, C. A. DeRosa, M. L. Daly, D. Song, M. Sabat and C. L. Fraser, *Mater. Chem. Front.*, 2017, **1**, 1866; (*d*) M. S. Kwon, J. Gierschner, J. Seo and S. Y. Park, *J. Mater. Chem. C*, 2014, **2**, 2552; (*e*) Y. Dong, J. Zhang, X. Tan, L. Wang, J. Chen, B. Li, L. Ye, B. Xu, B. Zou and W. Tian, *J. Mater. Chem. C*, 2013, **1**, 7554.

10 Little is known for the MCL of acid-exposed fluorophores. See: (*a*) S. Ito, C. Nishimoto and S. Nagai, *CrystEngComm*, 2019, **21**, 5699; (*b*) M. Kondo, T. Yamoto, S. Miura, M. Hashimoto, C. Kitamura and N. Kawatsuki, *Chem. – Asian J.*, 2019, **14**, 471; (*c*) P. Xue, P. Chen, J. Jia, Q. Xu, J. Sun, B. Yao, Z. Zhang and R. Lu, *Chem. Commun.*, 2014, **50**, 2569.

11 (*a*) M. Yamashita, S. Nagai, S. Ito and T. Tachikawa, *J. Phys. Chem. Lett.*, 2021, **12**, 7826; (*b*) S. Ito, S. Nagai, T. Ubukata and T. Tachikawa, *CrystEngComm*, 2021, **23**, 5899; (*c*) S. Takahashi, S. Nagai, M. Asami and S. Ito, *Mater. Adv.*, 2020, **1**, 708; (*d*) S. Ito, S. Nagai, T. Ubukata, T. Ueno and H. Uekusa, *Cryst. Growth Des.*, 2020, **20**, 4443; (*e*) S. Ito, S. Nagai, T. Ubukata and M. Asami, *Chem. Lett.*, 2019, **48**, 1492; (*f*) S. Nagai, M. Yamashita, T. Tachikawa, T. Ubukata, M. Asami and S. Ito, *J. Mater. Chem. C*, 2019, **7**, 4988.

12 A chloroform solution prepared from the crystals exposed to 6M HCl vapor for 30 min exhibited almost identical absorption and fluorescence spectra to those of a chloroform solution of non-protonated crystals (Fig. S9, ESI†).

13 A. P. Green and A. R. Buckley, *Phys. Chem. Chem. Phys.*, 2015, **17**, 1435.

14 S. I. Bezzubov, P. Kalle, A. A. Bilyalova, S. V. Tatarin and V. D. Dolzhenko, *Chem. – Eur. J.*, 2018, **24**, 12779.

15 S. J. N. Dixit, C. Gupta, T. H. Tadavi, K. R. S. Chandrakumar, S. Bose and N. Agarwal, *New J. Chem.*, 2021, **45**, 16238.

16 T. Gao, S. Yang, X. Cao, J. Dong, N. Zhao, P. Ge, W. Zheng and Z. Cheng, *Anal. Chem.*, 2017, **89**, 10085.

17 CrysAlisPro: Data Collection and Processing Software, Rigaku Corporation, Tokyo 196-8666, Japan, 2015.

18 A. Altomare, G. Cascarano, C. Giacovazzo and A. Guagliardi, *J. Appl. Crystallogr.*, 1993, **26**, 343.

19 CrystalStructure 4.2.5: Crystal Structure Analysis Package, Rigaku Corporation, Tokyo 196-8666, Japan, 2000-2017.

20 G. M. Sheldrick, *Acta Crystallogr., Sect. A: Found. Crystallogr.*, 2008, **64**, 112.

21 M. J. Frisch, G. W. Trucks, H. B. Schlegel, G. E. Scuseria, M. A. Robb, J. R. Cheeseman, G. Scalmani, V. Barone, G. A. Petersson, H. Nakatsuji, X. Li, M. Caricato, A. V. Marenich, J. Bloino, B. G. Janesko, R. Gomperts, B. Mennucci, H. P. Hratchian, J. V. Ortiz, A. F. Izmaylov, J. L. Sonnenberg, D. Williams-Young, F. Ding, F. Lipparini, F. Egidi, J. Goings, B. Peng, A. Petrone, T. Henderson, D. Ranasinghe, V. G. Zakrzewski, J. Gao, N. Rega, G. Zheng, W. Liang, M. Hada, M. Ehara, K. Toyota, R. Fukuda, J. Hasegawa, M. Ishida, T. Nakajima, Y. Honda, O. Kitao, H. Nakai, T. Vreven, K. Throssell, J. A. Montgomery, Jr., J. E. Peralta, F. Ogliaro, M. J. Bearpark, J. J. Heyd, E. N. Brothers, K. N. Kudin, V. N. Staroverov, T. A. Keith, R. Kobayashi, J. Normand, K. Raghavachari, A. P. Rendell, J. C. Burant, S. S. Iyengar, J. Tomasi, M. Cossi, J. M. Millam, M. Klene, C. Adamo, R. Cammi, J. W. Ochterski, R. L. Martin, K. Morokuma, O. Farkas, J. B. Foresman and D. J. Fox, *Gaussian 16, Revision A.03*, Gaussian, Inc., Wallingford CT, 2016.

22 D. Jacquemin, E. A. Perpète, G. E. Scuseria, I. Ciofini and C. Adamo, *J. Chem. Theory Comput.*, 2008, **4**, 123.